

THREE-DIMENSIONAL FLOW STRUCTURES OVER A LOW-ASPECT-RATIO PLUNGING WING

Berkan Anilir[1], Dilek Funda Kurtulus[1] & Max F. Platzer[2]

[1]Middle East Technical University, Aerospace Engineering Department, Ankara, Turkey
[2]University of California, Davis, Department of Mechanical and Aerospace Engineering, Davis, California, USA

Abstract

The objective of this study is to numerically investigate the three-dimensional flow structures over a sinusoidally plunging low-aspect-ratio NACA0012 wing ($sAR = 1$). The flow is analyzed by solving the URANS equations combined with the SST $\gamma - Re_\theta$ model to capture transitional effects across various Reynolds numbers ($Re = 5 \times 10^3 - 6 \times 10^4$) and nondimensional plunge velocities ($v_p = 1.05 - 3.14$). The results show that while mean thrust coefficient scales directly with v_p, propulsive efficiency behaves inversely. Interestingly, at higher frequencies, the 3D wing becomes more efficient than a 2D airfoil because tip-vortex-induced spanwise flow delays local dynamic stall over the mid-span. Furthermore, while 2D airfoils exhibit deflected wakes at high plunge velocities, the 3D finite wing maintains a symmetric reverse Karman vortex street across all conditions due to the symmetric circulation of its interconnected vortex loops and tip vortex.

Keywords: low-aspect-ratio wing, unsteady aerodynamics, micro air vehicles, plunging wing

1. Introduction

Low-aspect-ratio (LAR) wings are characterized by the nonlinear lift behavior with having considerably less lift-curve slope but greater stall angle of attack compared to high-aspect-ratio wings or two-dimensional airfoils. The wind tunnel experiments of Torres and Mueller [1] for various wing platforms (rectangular, Zimmerman, inverse Zimmerman) and aspect ratios ($AR = 0.5 - 2$) confirm these characteristics at $Re = 7.5 \times 10^4 - 2 \times 10^5$. Moreover, micro air vehicle (MAV) platforms frequently utilize low-aspect-ratio wings, as demonstrated by designs such as the Black Widow [2] and Bee [3]. Also, the operating Reynolds numbers of MAVs are in the range of between $10^3 - 10^5$, thus, it is important to explore these viscous dominated, transitional, low Reynolds number flow regimes. Since conventional fixed-wing designs experience significant performance losses in these regimes, one possible solution to this problem is flapping wing concept. However, effective implementation necessitates a fundamental understanding of the governing unsteady flow physics [4].

Calderon et al. [5] performed volumetric three-component velocimetry measurements and large eddy simulations (LES) on the plunging rectangular and elliptic flat plate wings with semi-aspect ratios of $sAR = 1$ and 2 at geometric angle of attack of 20° and Reynolds number of 2×10^4. The plunge amplitude (h_0) is set to $0.15c$, and the chord-based Strouhal (St_c) number ranges between 0 and 1.35. They examined the flow in the plunging motion cycle and observed the strong interactions between the wing tip, leading edge and trailing edge vortices. The aspect ratio and Strouhal number determine whether one or two arch vortices form, while high Strouhal numbers also generate a self-propelling tip vortex ring. The plunging rectangular flat plate with $AR = 2$ was studied by Visbal et al. [6], performing both water tunnel experiments and LES at a Reynolds number of 1×10^4. Numerical results demonstrate that the leading-edge vortex (LEV) evolves into a vertical arch structure positioned near the wing tip. This arch moves toward the wing's root, creating distinct cross-flow features consistent with experimental data. The same geometry but undergoing pitching motion at a wider range of Reynolds

numbers ($1 \times 10^3 - 2 \times 10^4$) was studied by Visbal [7]. He found that an increase in Reynolds number or pitch rate leads to greater maximum lift production, a more condensed arch vortex structure, stronger circulation and stall delay. Von Ellenrieder et al. [8] examined the three-dimensional flow structure over the pitching and plunging rectangular finite wing with $AR = 3$ by dye visualization at a Reynolds number of 164, and several interconnected vortex rings were observed. Several additional studies in the literature are likely to be useful for readers interested in the aerodynamics of flapping finite wings [9, 10, 11, 12, 13, 14, 15, 16, 17, 18, 19].

The objective of the current study is to investigate three-dimensional flow structures over sinusoidally plunging low-aspect-ratio wing ($sAR = 1$) dominated by strong wing tip vortex and vortices shed from leading edge and trailing edge. To this end, the configuration is analyzed by solving Unsteady Reynolds-averaged Navier-Stokes (URANS) equations and using the shear stress transport (SST) $\gamma - Re_\theta$ turbulence model at various Reynolds numbers ($Re = 5 \times 10^3 - 6 \times 10^4$) and nondimensional plunge velocities ($v_p = 1.05 - 3.14$).

2. Methodology

The three-dimensional, unsteady and incompressible flow over a sinusoidally plunging finite rectangular wing of half-span $b = 0.1m$ and chord length $c = 0.1m$, with a NACA0012 airfoil is examined in this study. The semi-aspect ratio of the wing is set to a low value of $sAR = b/c = 1$, while the reference area becomes $S = 0.01m$ (see Figure 1). The wing exhibits 0° geometric angle of attack during its motion. To reduce computational cost, a half-wing model is utilized with a symmetry boundary condition applied at the wing root. Also, the wing has a sharp trailing edge and a straight-cut wing tip. The unsteady computations are performed as the plunging wing undergoes a periodic plunging motion given by Eq. 1. The fluid domain is prescribed as water-liquid at 15 °C. The wide range of chord and freestream velocity (U_∞) based Reynolds numbers ($Re = \rho U_\infty c/\mu$) between 5×10^3 and 6×10^4 are studied. The plunge amplitude is set to $h_0 = 0.05c$. The plunge frequencies vary between $f = 5$ Hz to $f = 20$ Hz with 5 Hz increment, while the corresponding nondimensional plunge velocity values are between $v_p = 1.05$ and $v_p = 3.14$.

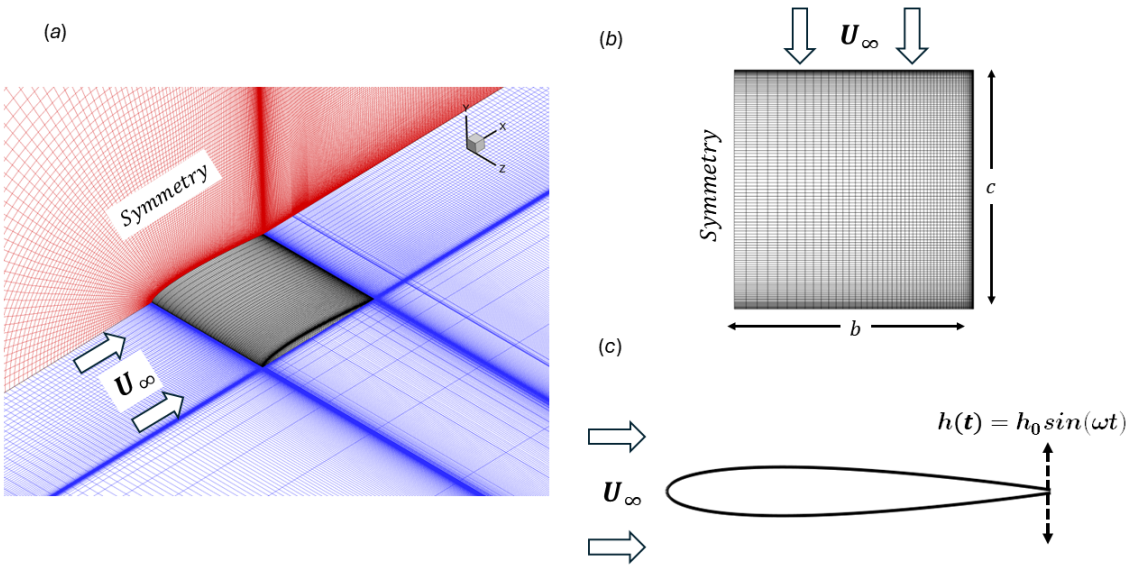


Figure 1 – (a) Computational domain (b) wing's surface grid and (c) schematic diagram of plunging motion

.

Eqs. 1 and 2 describe the plunging wing kinematics in terms of the sinusoidal vertical position ($h(t)$) and angular frequency (ω):

$$h(t) = h_0 \sin(\omega t) \tag{1}$$

$$\omega = 2\pi f \tag{2}$$

where h_0 represents the plunge amplitude and f denotes the plunge frequency in Hz. The plunging motion is described by the reduced frequency (k) and the nondimensional plunge velocity (v_p), given in Eqs. 3 and 4:

$$k = \frac{\omega c}{U_\infty} \tag{3}$$

$$v_p = k\left(\frac{h_0}{c}\right) \tag{4}$$

Propulsive efficiency (η) is defined as the ratio of the mean thrust coefficient ($\overline{C_t}$) to the mean power coefficient ($\overline{C_P}$), as shown in Eqs. 5–7:

$$\eta = \frac{\overline{C_t}}{\overline{C_P}} \tag{5}$$

$$\overline{C_T} = \frac{\overline{T}}{0.5\rho U_\infty^2 S} \tag{6}$$

$$\overline{C_P} = \frac{1}{\Delta t}\int_{\Delta t}\left(\frac{C_l \dot{h}}{U_\infty}\right) dt \tag{7}$$

where $\overline{T}$ is the mean thrust force, ρ is the fluid density and C_l is the instantaneous lift coefficient. Time-averaged values are determined by averaging five periods once periodic conditions are established.

2.1 Numerical Methodology

Simulations are conducted in ANSYS Fluent v17.2 solving the URANS equations with the SST $\gamma - Re_\theta$ turbulence model. The Least Squares Cell-Based scheme is used for gradient evaluation, and all governing equations are discretized using a second-order upwind scheme. For time advancement, the second-order implicit iterative time advancement scheme (ITA) was used to maintain a CFL number ≤ 10 ($CFL = u\Delta t/\Delta x$). Pressure-velocity coupling is done by a segregated type algorithm of PISO (Pressure-Implicit with Splitting of Operators), and the details of the algorithm can be found in [20]. The flow field is modeled using the unsteady, incompressible Navier-Stokes equations. In Cartesian tensor notation, the conservation of mass and momentum are expressed as:

$$\frac{\partial U_j}{\partial x_j} = 0 \tag{8}$$

$$\frac{\partial U_i}{\partial t} + \frac{\partial}{\partial x_j}(U_j U_i) = -\frac{1}{\rho}\frac{\partial p}{\partial x_i} + \frac{\partial}{\partial x_j}\left[\nu_{\text{eff}}\left(\frac{\partial U_i}{\partial x_j} + \frac{\partial U_j}{\partial x_i}\right)\right] \tag{9}$$

where U represents the velocity vector, p is the static pressure, and ν_{eff} denotes the effective kinematic viscosity, which is defined as the sum of molecular kinematic viscosity (ν) and turbulent eddy viscosity (ν_t). To close the Reynolds-averaged Navier-Stokes (RANS) equations, the $k-\omega$ Shear Stress Transport (SST) model proposed by Menter [21] is employed. This model solves two transport equations: one for the turbulent kinetic energy (k) and another for the specific dissipation rate (ω), given in Eqs. 10 and 11:

$$\frac{\partial k}{\partial t} + \frac{\partial}{\partial x_j}(U_j k) = \widetilde{P}_k - \beta^* k\omega + \frac{\partial}{\partial x_j}\left[(\nu + \sigma_k \nu_t)\frac{\partial k}{\partial x_j}\right] \tag{10}$$

$$\frac{\partial \omega}{\partial t} + \frac{\partial}{\partial x_j}(U_j \omega) = \frac{\gamma_\omega}{\nu_t}\widetilde{P}_k - \beta\omega^2 + \frac{\partial}{\partial x_j}\left[(\nu + \sigma_\omega \nu_t)\frac{\partial \omega}{\partial x_j}\right] + 2(1-F_1)\frac{\sigma_{\omega 2}}{\omega}\frac{\partial k}{\partial x_j}\frac{\partial \omega}{\partial x_j} \tag{11}$$

The turbulent eddy viscosity is subsequently calculated using the definition in Eq. 12:

$$\nu_t = \frac{a_1 k}{\max(a_1\omega, \Omega F_2)} \tag{12}$$

In these expressions, $\widetilde{P}_k$ represents the production rate of turbulent kinetic energy ($2\nu_t S_{ij} S_{ij}$), where S_{ij} and Ω_{ij} are the strain-rate and rotation-rate tensors, respectively. The formulation utilizes blending functions F_1 and F_2 to switch between turbulence models. Specifically, F_1 modulates the solution behavior where it approaches unity in the near-wall region, activating the standard $k-\omega$ model, and shifts to zero in the free shear layer, recovering the $k-\varepsilon$ model behavior [21]. To accurately predict laminar-to-turbulent transition, the baseline SST model is augmented with the $\gamma - Re_{\theta t}$ transition model developed by Langtry and Menter [22]. This model introduces two additional transport equations for intermittency (γ) and the transition momentum thickness Reynolds number ($\hat{Re}_{\theta t}$):

$$\frac{\partial \gamma}{\partial t} + \frac{\partial}{\partial x_j}(U_j \gamma) = \widetilde{P}_\gamma - \widetilde{E}_\gamma + \frac{\partial}{\partial x_j}\left[\left(\nu + \frac{\nu_t}{\sigma_f}\right)\frac{\partial \gamma}{\partial x_j}\right] \tag{13}$$

$$\frac{\partial \hat{Re}_{\theta t}}{\partial t} + \frac{\partial}{\partial x_j}(U_j \hat{Re}_{\theta t}) = \widetilde{P}_{\theta t} + \frac{\partial}{\partial x_j}\left[\left(\nu + \frac{\nu_t}{\sigma_{\theta t}}\right)\frac{\partial \hat{Re}_{\theta t}}{\partial x_j}\right] \tag{14}$$

where $\widetilde{P}_\gamma$ and $\widetilde{E}_\gamma$ are the source and destruction terms for intermittency, respectively, while $\widetilde{P}_{\theta t}$ serves as the source term for the transition momentum thickness Reynolds number equation. The intermittency variable γ triggers the onset of transition ($\gamma > 0$), whereas the $\hat{Re}_{\theta t}$ equation correlates local flow parameters to the critical Reynolds number where transition begins. Although this approach does not resolve the physics of laminar-to-turbulent transition, it effectively models both natural and bypass transition phenomena within the RANS framework [22, 23]. The model has been applied and validated in the literature at low Reynolds number flows by Counsil and Boulama [24], Zore et al. [23], Anilir et al. [25, 26, 27, 28], and Guney et al. [29].

Figures 1a and 1b show the computational domain on the external part and on the surface of the wing, respectively. The grid refinement study was performed for the stationary wing at $Re = 4\times10^4$ and $\alpha = 20^\circ$ in our previous study Anilir et al. [25] and the fully structured grid with $360\times340\times95$ size, which corresponds to total number of element of around 12×10^6, was selected. The domain dimensions are $(x/c,\, y/c,\, z/c) \in [-15,15]\times[-15,15]\times[0,11]$, with the origin at the wing root leading edge. The mesh utilizes a first cell height of $\Delta s = 0.001c$ to ensure $y^+ < 1$ (Figure 2). Boundary conditions include a velocity inlet ($U = (U_\infty, 0, 0)$) at the inlet and farfield, and a pressure outlet downstream to facilitate wake convection. Symmetry is enforced at the wing root plane, with a no-slip condition on the wing surface.

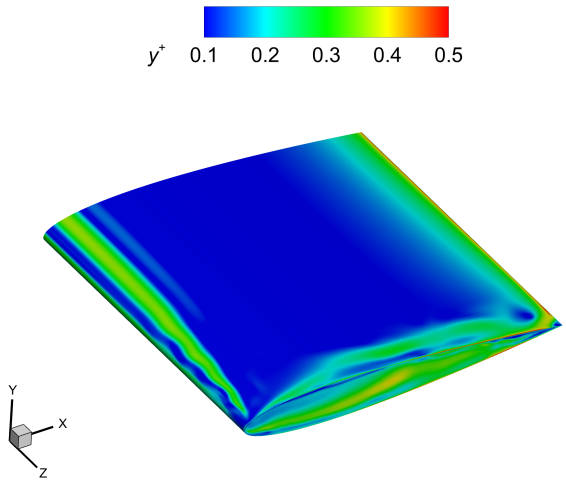


Figure 2 – y^+ contours at $Re = 4\times10^4$ and $v_p = 1.57$

3. Results and Discussion

Table 1 displays the values of freestream velocity, flapping frequency, Reynolds number, the reduced frequency and nondimensional plunge velocity that were selected to examine the three-dimensional flow structures over the low-aspect-ratio plunging wing. As shown in the table, the flapping frequency is adjusted according to the freestream velocity to maintain constant reduced frequency and nondimensional plunge velocity for each case.

Table 1 – Configuration summary

Case	U_∞ **[m/s]**	f **[Hz]**	Re	k	v_p
C1	$0.05-0.2$	$5-20$	$5\times10^3-2\times10^4$	62.83	3.14
C2	$0.1-0.4$	$5-20$	$1\times10^4-4\times10^4$	31.42	1.57
C3	$0.15-0.6$	$5-20$	$1.5\times10^4-6\times10^4$	20.94	1.05

3.1 Aerodynamic Forces and Propulsive Efficiency

Figure 3 shows the mean thrust coefficient and propulsive efficiency with respect to the plunge frequency for both three-dimensional low-aspect-ratio finite wing and airfoil. Across both 2D and 3D configurations, $\overline{C_T}$ exhibits a strong positive correlation with v_p as expected, while the highest thrust values are consistently achieved at $v_p = 3.14$. As the effective angle of attack is defined, $\alpha_{eff} = arctan(v_p)$, the strong leading edge vortices form at high v_p due to exceeding the dynamic stall limits. While leading edge vortices typically degrade thrust generation in high-Reynolds number regimes, their negative effect is heavily counteracted by the intensified trailing edge vortices at low Reynolds numbers; consequently, the net thrust continues to scale directly with v_p despite any LEV induced losses [28]. For a given v_p, $\overline{C_T}$ remains relatively flat or exhibits only a minor upward trend as the plunge frequency ranges from 5 Hz to 20 Hz (accompanied by an increase in Re). This implies that within our simulation conditions, the kinematic parameter v_p is the primary governing parameter of the mean thrust magnitude. It is also evident that the 2D plunging airfoil generates significantly larger thrust, reaching almost twice that of the LAR wing.

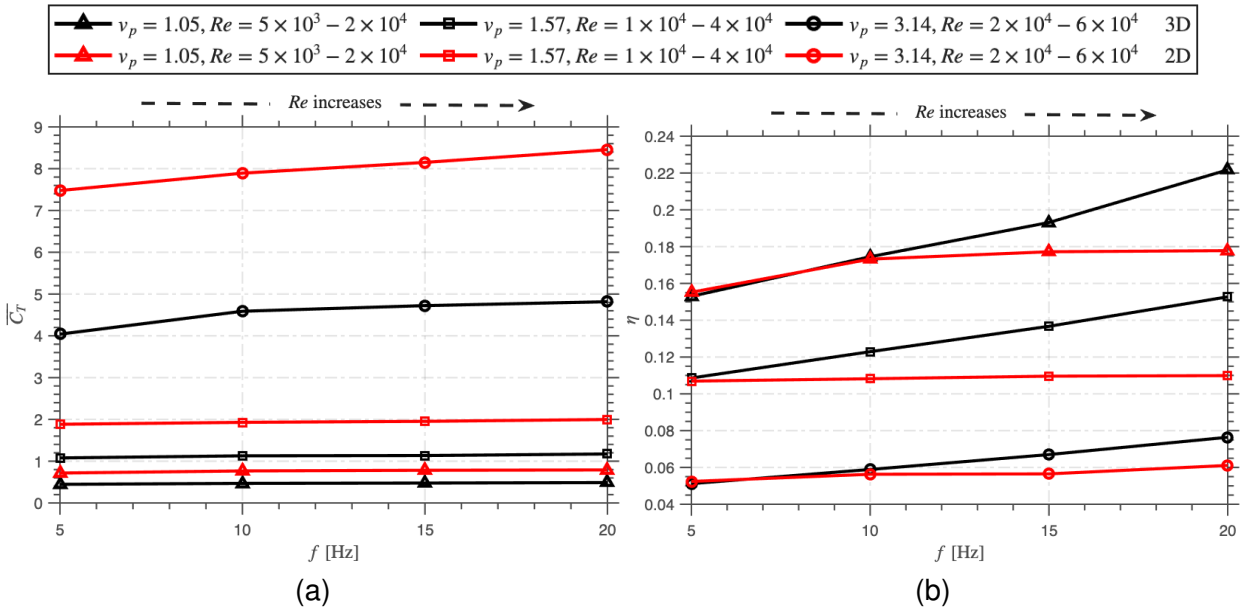


Figure 3 – Variation of (a) mean thrust coefficient and (b) propulsive efficiency with respect to plunge frequency

.

Contrary to the thrust coefficient, the propulsive efficiency behaves inversely with respect to v_p. The lowest dimensionless velocity ($v_p = 1.05$) yields the highest efficiency peaks ($\eta \approx 0.15 - 0.22$), whereas the high-thrust condition ($v_p = 3.14$) drops significantly below $\eta = 0.08$. The peak in propulsive efficiency is frequently observed between $v_p = 0.2$ and $v_p = 0.5$, and then drastically decreases [30, 28, 31, 32]. So there is a trade-off in flapping-wing configurations that high v_p leads to massive flow separation, resulting in high thrust but high power requirements. On the other hand, low v_p operates in a more streamlined, attached flow, optimizing aerodynamic efficiency. An interesting result is examined in the efficiency plots as frequency and Reynolds number increase. The efficiency curves for the 2D airfoil flatten out early. However, the 3D LAR wing curves show a steady, continuous increase. At higher frequencies ($f \geq 10$ Hz), the 3D LAR wing actually becomes more efficient than the 2D airfoil for both $v_p = 1.05$ and $v_p = 1.57$. This behavior can be attributed to the following factors. In pure plunging motion, 2D airfoils suffer from strong dynamic stall and large flow separation, which creates a high drag penalty. On the other hand, the 3D LAR wing ($sAR = 1$) generates strong tip vortices that influence a large portion of the spanwise flow. This spanwise flow helps by moving vorticity toward the wingtips, thereby reducing local dynamic stall and delaying flow separation over the middle of the wing. As a result, the power needed to move the 3D finite wing drops faster than its thrust drops. This leads to a higher net efficiency than the 2D airfoil at high frequencies and Reynolds numbers.

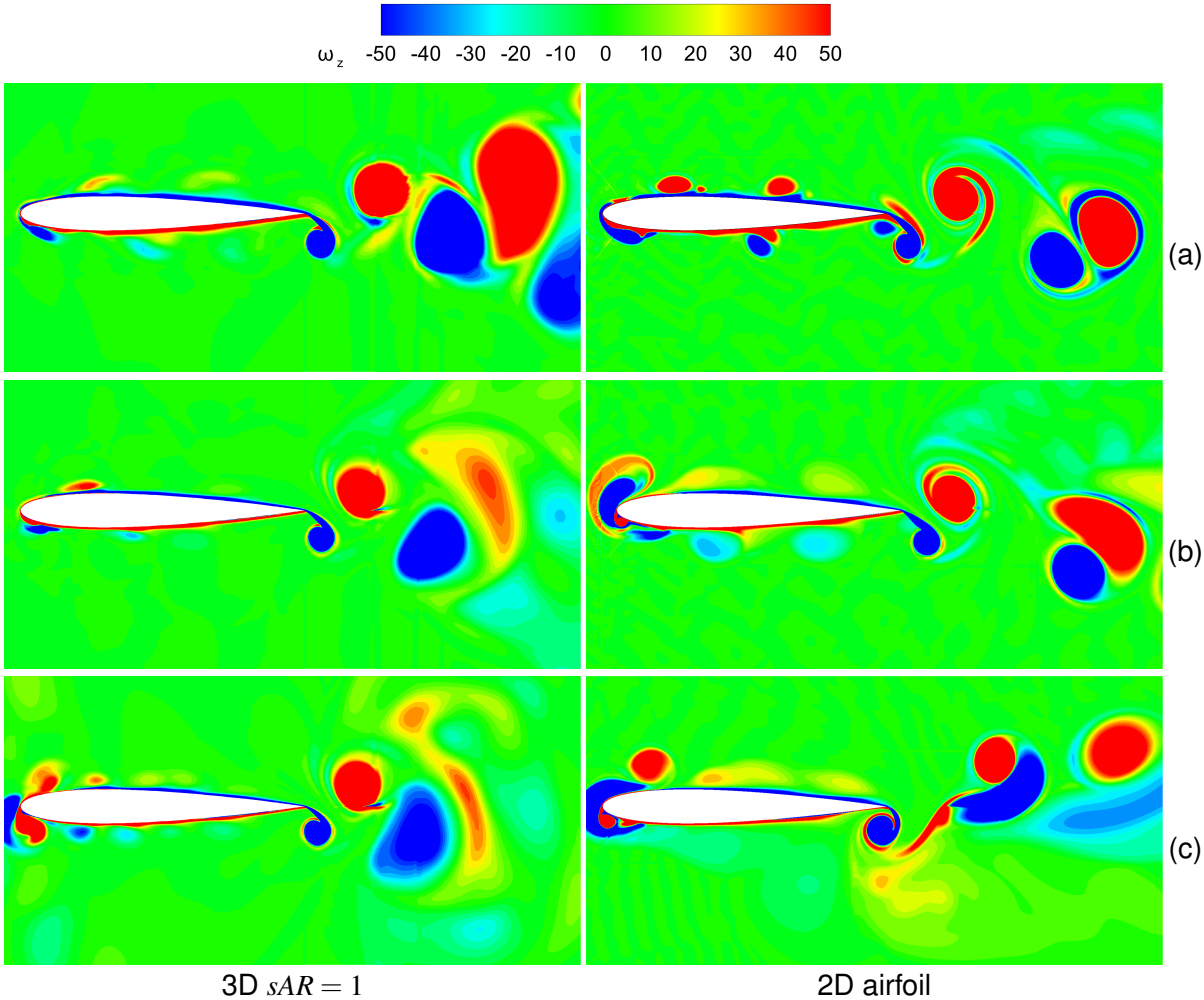


Figure 4 – Instantaneous vorticity field at (a) $v_p = 1.05$ ($f = 20$ Hz, $Re = 6 \times 10^4$), (b) $v_p = 1.57$ ($f = 10$ Hz, $Re = 2 \times 10^4$) and (c) $v_p = 3.14$ ($f = 10$ Hz, $Re = 1 \times 10^4$) for finite wing at the spanwise slice of $z/c = 0.1$ and two-dimensional airfoil

.

3.2 Evolution of Vortical Structures and Wake Deflection

In this study, high nondimensional plunge velocities are examined, and one feature of these conditions is a deflected wake [12, 33, 34]. The trailing edge vortices are shed in pairs and move at an angle to the main flow direction. This causes the wake to deflect, breaking symmetry even when the angle of attack is zero. Research shows that this deflection is an inviscid process, meaning that leading edge separation is not required for this formation [33]. Once the wake deflects, its direction (either up or down) remains stable and constant. This direction is decided entirely by the initial direction of the movement. Figure 4 illustrates the vortical structures over the spanwise slice of the three-dimensional wing near the root and two-dimensional airfoil at various nondimensional plunge velocities. It can be clearly seen that the clockwise trailing edge vortex pairs with the counter-clockwise trailing edge vortex from the following half cycle and shed towards the opposite side of the initial upward movement of the airfoil for $v_p = 1.05$ and $v_p = 1.57$. As v_p is further increased to 3.14, the vortices again form a pair; however, this pair does not deflect and instead sheds almost parallel to the freestream. On the other hand, the symmetric reverse Karman vortex street is observed for the three-dimensional wing regardless of the nondimensional plunge velocity, and this indicates inhibited deflected jets by finite wings. Calderon et al. [12]'s water tunnel experiments on the finite wing of $sAR = 3$ finite wing and the effectively infinite wing also confirmed that the finite wings prevent deflected wake phenomenon. They have two explanations for this behaviour. The first is that the tip vortex creates a three-dimensional flowfield that prevents the vortices from pairing up. The second is that the interconnected vortex loops have symmetric circulation due to the physical topology of a finite wing. This symmetry was confirmed by their circulation measurements.

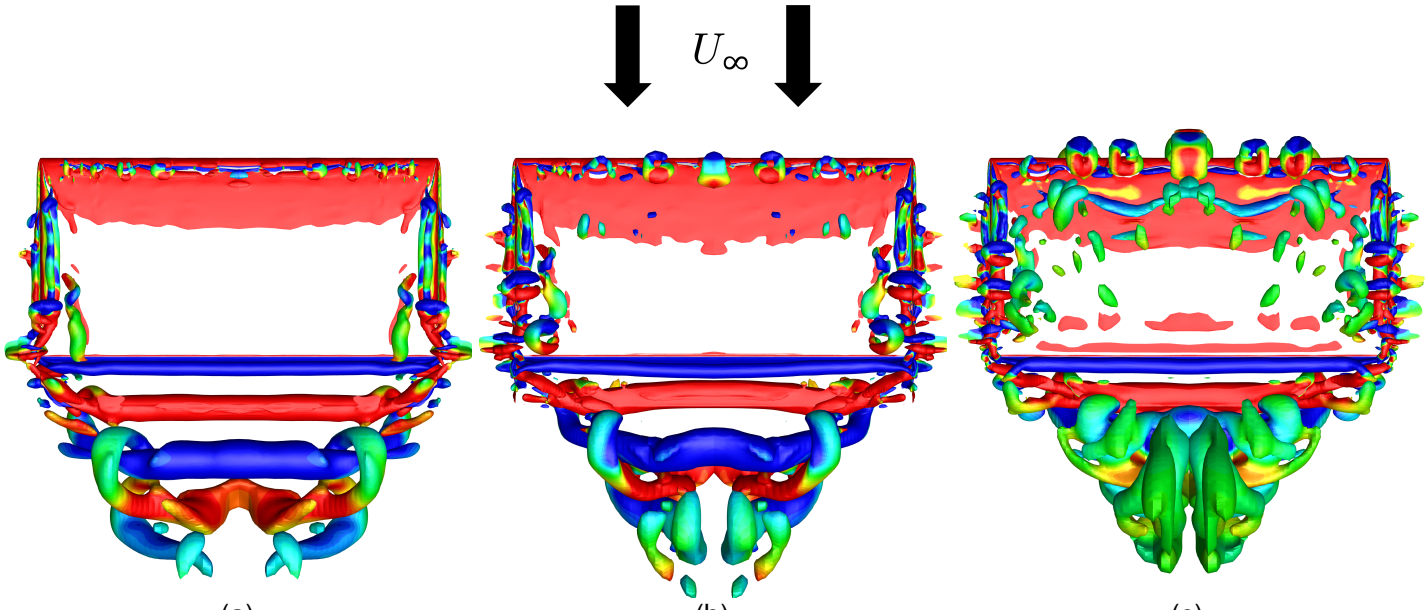


Figure 5 – Top view of the vortical structure for $v_p = 1.05$ ($f = 10$ Hz, $Re = 3 \times 10^4$), (b) $v_p = 1.57$ ($f = 20$ Hz, $Re = 4 \times 10^4$) and (c) $v_p = 3.14$ ($f = 15$ Hz, $Re = 1.5 \times 10^4$). The isosurface of $Q^* = Qc^2/U_\infty^2 = 10$ is visualised and coloured with spanwise vorticity contours in the range -50 to 50, from red to blue. The full span wings are displayed for better visualization by applying a mirror on the root.

.

Figure 5 shows the top view of the three-dimensional vortical structures around a plunging finite wing at different nondimensional plunge velocity amplitudes. The flow fields are visualized using nondimensional Q-criterion isosurfaces ($Q^* = 10$) and colored by spanwise vorticity contours. Looking at the cases from left to right, the effects of increasing v_p on the wake behavior and the leading-edge flow structures are clearly observed. For the $v_p = 1.05$ case, the leading-edge vortex appears relatively uniform and stable across the span. The wake structures in the downstream region exhibit a clear, smooth vortex topology where the tip vortices interact with the trailing-edge structures to

form connected loops. Similar interconnected vortex loops were observed by Calderon et al. [12] at $v_p = 1.91$ and $Re = 1 \times 10^4$ for a finite NACA0012 wing with $sAR = 3$; they explained this topology as one of the main driving factors for symmetrical wake formation behind finite plunging wings. As v_p increases to 1.57, small-scale instabilities begin to appear near the leading edge. The LEVs begin to break down into smaller, separated shear layer vortices. In the wake, the vortex structures are more compressed and display more complex, three-dimensional twisting. At the highest plunging velocity of $v_p = 3.14$, the flow transitions into a highly unstable state characterized by the formation of large vortical structures near both the wing tip and the leading edge. The leading edge region is dominated by distinct, repetitive vortex rings due to strong shear layer breakdown and a high effective angle of attack ($\alpha_{eff}(3.14) = 72.3°$). Interestingly, as discussed previously, when v_p reaches 3.14, the wake structures do not deflect. Instead, the vortices remain symmetric and shed straight along the neutral line of the wing.

4. Conclusion

In this study, the unsteady, three-dimensional incompressible flow over a sinusoidally plunging low-aspect-ratio NACA0012 wing ($sAR = 1$) was numerically investigated using a SST $\gamma - Re_\theta$ turbulence model. The effects of nondimensional plunge velocity and Reynolds number on thrust generation, propulsive efficiency, and vortex topology were evaluated. The kinematic parameter v_p was found to be the primary driver of thrust magnitude, with the highest thrust achieved at $v_p = 3.14$ due to strong leading-edge vortex formation. Although the two-dimensional plunging airfoil generates greater net thrust, the three-dimensional finite wing achieves superior propulsive efficiency at higher plunge frequencies. This performance benefit occurs because tip vortices induce spanwise flow that relieves deep dynamic stall over the central portion of the wing, lowering the required power input. Finally, visualization of the wake confirms that the three-dimensional wing suppresses the wake deflection phenomenon observed in two-dimensional flows. Due to the symmetric topology and interconnected nature of the tip and trailing-edge vortices, the finite wing maintains a symmetric, non-deflected wake along the neutral line across all simulated conditions.

5. Contact Author Email Address

Corresponding author's email adress: anilir.berkan@metu.edu.tr

6. Copyright Statement

The authors confirm that they, and/or their company or organization, hold copyright on all of the original material included in this paper. The authors also confirm that they have obtained permission, from the copyright holder of any third party material included in this paper, to publish it as part of their paper. The authors confirm that they give permission, or have obtained permission from the copyright holder of this paper, for the publication and distribution of this paper as part of the ICAS proceedings or as individual off-prints from the proceedings.

References

[1] G. E. Torres and T. J. Mueller. Low-Aspect-Ratio Wing Aerodynamics at Low Reynolds Numbers. *AIAA Journal*, 43(5):865–873, 2004.

[2] J. M. Grasmeyer and M. T. Keennon. Development of the Black Widow Micro Air Vehicle. In *39th Aerospace Sciences Meeting and Exhibit*, page 0127, 2001.

[3] K. Sibilski, M. Nowakowski, D. Rykaczewski, P. Szczepaniak, A. Zyluk, A. Sibilska-Mroziewicz, M. Garbowski, and W. Wróblewski. Identification of Fixed-Wing Micro Aerial Vehicle Aerodynamic Derivatives from Dynamic Water Tunnel Tests. *Aerospace*, 7(8):116, 2020.

[4] M. F. Platzer, D. F. Kurtulus, and B. Anilir. *Low Speed Wing Aero-Hydrodynamics : Emission-Free Lift, Thrust, and Power Generation*. Springer Switzerland, 2026.

[5] D. E. Calderon, Z. Wang, I. Gursul, and M. R. Visbal. Volumetric measurements and simulations of the vortex structures generated by low aspect ratio plunging wings. *Physics of Fluids*, 25:067102, 2013.

[6] M. Visbal, T. O. Yilmaz, and D. Rockwell. Three-dimensional vortex formation on a heaving low-aspect-ratio wing: Computations and experiments. *Journal of Fluids and Structures*, 38:58–76, 2013.

[7] M. R. Visbal. Unsteady flow structure and loading of a pitching low-aspect-ratio wing. *Physical Review Fluids*, 2(024703), 2017.

[8] K. D. von Ellenrieder, K. Parker, and J. Soria. Flow structures behind a heaving and pitching finite-span wing. *Journal of Fluid Mechanics*, 490:129–138, 2003.

[9] J. H. J. Buchholz and A. Smits. On the evolution of the wake structure produced by a low-aspect-ratio pitching panel. *Journal of Fluid Mechanics*, 546:433–443, 2006.

[10] H. J. Dong, R. Mittal, and F. M. Najjar. Wake topology and hydrodynamic performance of low-aspect-ratio flapping foils. *Journal of Fluid Mechanics*, 566:309–343, 2006.

[11] T. O. Yilmaz and D. Rockwell. Three-dimensional flow structure on a maneuvering wing. *Experiments in Fluids*, 48:539–544, 2010.

[12] D. E. Calderon, Z. Wang, I. Gursul, and M. R. Visbal. n the Absence of Asymmetric Wakes for Periodically Plunging Finite Wings. *Physics of Fluids*, 26(7):071907, 2014.

[13] D. J. Cleaver, D. E. Calderon, Z. Wang, and I. Gursul. Lift enhancement through flexibility of plunging wings at low Reynolds numbers. *Journal of Fluids and Structures*, 64:27–45, 2016.

[14] I. Gursul and D. Cleaver. Plunging Oscillations of Airfoils and Wings: Progress, Opportunities, and Challenges. *AIAA Journal*, 57(9):3648–3665, 2019.

[15] M. R. Visbal and D. J. Garmann. Dynamic Stall of a Finite-Aspect-Ratio Wing. *AIAA Journal*, 57(3):962–977, 2019.

[16] N. Chiereghin, S. Bull, D. J. Cleaver, and I. Gursul. Three-dimensionality of leading-edge vortices on high aspect ratio plunging wings. *Physical Review Fluids*, 5(064701), 2020.

[17] O. Son, A.-K. Gao, I. Gursul, C. D. Cantwell, Z. Wang, and S. J. Sherwin. Three-dimensionality of leading-edge vortices on high aspect ratio plunging wings. *Journal of Fluid Mechanics*, 940(A28), 2022.

[18] O. Son, Z. Wang, and I. Gursul. Dynamics of tip vortices on plunging wings. *Aerospace Science and Technology*, 128(107761), 2022.

[19] O. Son, Z. Wang, and I. Gursul. Effect of wing planform on plunging wing aerodynamics. *Journal of Fluids and Structures*, 121(103953), 2023.

[20] J. H. Ferziger, M. Perić, and R. L. Street. *Computational Methods for Fluid Dynamics*. Springer Switzerland, 4th edition, 2020.

[21] F. R. Menter. Two-equation eddy-viscosity turbulence models for engineering applications. *AIAA Journal*, 32(8):1598–1605, 1994.

[22] R. B. Langtry and F. R. Menter. Correlation-based transition modeling for unstructured parallelized computational fluid dynamics codes. *AIAA Journal*, 47(12):2894–2906, 2009.

[23] K. Zore, A. Matyushenko, S. Shah, C. Aliaga, J. Stokes, and F. Menter. Laminar–Turbulent Transition Prediction on Industrial Computational Fluid Dynamics Applications. *AIAA Journal*, 60(1):1–20, 2023.

[24] J. N. N. Counsil and K. G. Boulama. Low-reynolds-number aerodynamic performances of the NACA 0012 and Selig–Donovan 7003 airfoils. *Journal of Aircraft*, 50(1):204–216, 2013.

[25] B. Anilir, K. Taiba, D. F. Kurtulus, S. Goli, M. Sabih, I. H. Imran, A. Memon, and L. M. Alhems. Transitional separated flow over low-aspect-ratio NACA0012 wings. *IEEE Access*, 14:21432–21445, 2026.

[26] B. Anilir, D. F. Kurtulus, and M. F. Platzer. Aerodynamics of Close-coupled Stationary/Flapping Tandem NACA 0012 Airfoils. In *39th Aerospace Sciences Meeting and Exhibit*, page 0127, 2001.

[27] B. Anilir, D. F. Kurtulus, and M. F. Platzer. Aerodynamics of Close-coupled Stationary/Flapping Tandem NACA 0012 Airfoils. In *AIAA Aviation Forum*, San Diego, CA, June 2023.

[28] B. Anilir, D. F. Kurtulus, and M. F. Platzer. Thrust Aerodynamics of Tractor/PusherTandem NACA0012 Airfoils at LowReynolds Numbers. *AIAA Journal*, 64(3):1740–1744, 2026.

[29] M. Guney, B. Anilir, and D. F. Kurtulus. Computational investigation of low-Reynolds-number unsteady flows past NACA 0012. *Progress in Computational Fluid Dynamics, an International Journal*, 26(1):32 – 47, 2026.

[30] B. Anilir, D. F. Kurtulus, and M. F. Platzer. Flow control by oscillating trailing-edge flaps. *AIAA Journal*, 61(9):4210–4213, 2023.

[31] J. Young and J. C. S. Lai. Mechanisms Influencing the Efficiency of Oscillating Airfoil Propulsion. *AIAA Journal*, 45(7):1695–1702, 2007.

[32] S. Heathcote, Z. Wang, and I. Gursul. Effect of spanwise flexibility on flapping wing propulsion. *Journal of Fluids and Structures*, 24(2):183–199, 2008.

[33] K. D. Jones, C. M. Dohring, and M. F. Platzer. Experimental and Computational Investigation of the Knoller-Betz Effect. *AIAA Journal*, 36(7):1240–1246, 1998.

[34] D. J. Cleaver, Z. Wang, and I. Gursul. Bifurcating Flows of Plunging Airfoils at High Strouhal Numbers.

Journal of Fluid Mechanics, 708:349–376, 2012.